



HAL
open science

Probing cosmology via the clustering of critical points

Junsup Shim, Christophe Pichon, Dmitri Pogosyan, Stephen Appleby,
Corentin Cadiou, Juhan Kim, Katarina Kraljic, Changbom Park

► **To cite this version:**

Junsup Shim, Christophe Pichon, Dmitri Pogosyan, Stephen Appleby, Corentin Cadiou, et al.. Probing cosmology via the clustering of critical points. *Monthly Notices of the Royal Astronomical Society*, 2024, 528 (2), pp.1604-1614. 10.1093/mnras/stae151 . hal-04324116

HAL Id: hal-04324116

<https://hal.science/hal-04324116v1>

Submitted on 25 Jan 2024








HAL is a multi-disciplinary open access archive for the deposit and dissemination of scientific research documents, whether they are published or not. The documents may come from teaching and research institutions in France or abroad, or from public or private research centers.

L'archive ouverte pluridisciplinaire **HAL**, est destinée au dépôt et à la diffusion de documents scientifiques de niveau recherche, publiés ou non, émanant des établissements d'enseignement et de recherche français ou étrangers, des laboratoires publics ou privés.



Distributed under a Creative Commons Attribution 4.0 International License

Probing cosmology via the clustering of critical points

Junsup Shim ¹★, Christophe Pichon ^{2,3,4}, Dmitri Pogosyan ⁵, Stephen Appleby ^{6,7},
Corentin Cadiou ⁸, Juhan Kim ⁹, Katarina Kraljic ¹⁰ and Changbom Park²

¹*Institute of Astronomy and Astrophysics, Academia Sinica, No.1, Section 4, Roosevelt Road, Taipei 10617, Taiwan*

²*School of Physics, Korea Institute for Advanced Study, 85 Hoegi-ro, Dongdaemun-gu, Seoul 02455, Republic of Korea*

³*CNRS and Sorbonne Université, Institut d'Astrophysique de Paris, UMR 7095, 98 bis Boulevard Arago, F-75014 Paris, France*

⁴*CNRS, CEA, Institut de physique théorique, Université Paris-Saclay, F-91191 Gif-sur-Yvette, France*

⁵*Department of Physics, University of Alberta, 11322-89 Avenue, Edmonton, Alberta T6G 2G7, Canada*

⁶*Asia Pacific Center for Theoretical Physics, Pohang 37673, Republic of Korea*

⁷*Department of Physics, POSTECH, Pohang 37673, Republic of Korea*

⁸*Lund Observatory, Division of Astrophysics, Department of Physics, Lund University, Box 43, SE-221 00 Lund, Sweden*

⁹*Center for Advanced Computation, Korea Institute for Advanced Study, 85 Hoegiro, Dongdaemun-gu, Seoul 02455, Republic of Korea*

¹⁰*Observatoire Astronomique de Strasbourg, Université de Strasbourg, CNRS, UMR 7550, F-67000 Strasbourg, France*

Accepted 2024 January 11. Received 2024 January 11; in original form 2023 November 16

ABSTRACT

Exclusion zones in the cross-correlations between critical points (peak-void, peak-wall, filament-wall, and filament-void) of the density field define quasi-standard rulers that can be used to constrain dark matter and dark energy cosmological parameters. The average size of the exclusion zone is found to scale linearly with the typical distance between extrema. The latter changes as a function of the matter content of the universe in a predictable manner, but its comoving size remains essentially constant in the linear regime of structure growth on large scales, unless the incorrect cosmology is assumed in the redshift–distance relation. This can be used to constrain the dark energy parameters when considering a survey that scans a range of redshifts. The precision of the parameter estimation is assessed using a set of cosmological simulations, and is found to be a 4σ detection of a change in matter content of 5 per cent, or about 3.8σ detection of 50 per cent shift in the dark energy parameter using a full sky survey up to redshift 0.5.

Key words: methods: analytical – methods: data analysis – methods: statistical – large-scale structure of Universe.

1 INTRODUCTION

The large-scale matter distribution is a valuable source of information because its clustering properties are sensitive to cosmology. Indeed, stringent constraints have been set on cosmological parameters thanks to measurements of the baryonic acoustic oscillation (e.g. Eisenstein et al. 2005; Percival et al. 2007; Okumura et al. 2008; Beutler et al. 2011; Dawson et al. 2013; Alam et al. 2021; Xu et al. 2023), redshift–space distortions (e.g. Da Ângela, Outram & Shanks 2005; Marinoni & Buzzi 2010; Okumura et al. 2016; Neveux et al. 2020), and Alcock–Paczynski effect (e.g. Blake et al. 2011; Li et al. 2016, 2018; Beutler et al. 2017; Zhang, Huang & Li 2019; Dong et al. 2023) in the two-point correlation functions of galaxies. However, as the evolution of the density field becomes increasingly non-linear, it departs from its Gaussian initial state. This causes an increasing amount of information to be contained in statistics beyond the two-point functions, which can be captured by measuring three-point correlation functions (e.g. Peebles & Groth 1975; Hinshaw et al. 1995; Nichol et al. 2006; Marín et al. 2013; Slepian et al. 2017; Sugiyama et al. 2023) or higher order moments (e.g. Fry 1985; Bouchet et al. 1993; Bernardeau 1994; Croton et al. 2004; Cappi

et al. 2015; Sabiu et al. 2019; Philcox, Hou & Slepian 2021; Philcox 2022; Hou, Slepian & Cahn 2023). While the hierarchy typically converges, each extra order becomes increasingly more difficult to measure robustly. This has fostered the development of alternative probes to obtain information beyond the simple two-point functions.

One avenue is to weigh the tracers used to compute the correlation functions according to their properties – such as the local density or galaxy properties – to obtain so-called marked statistics (White & Padmanabhan 2009; Uhlemann et al. 2017; Armijo et al. 2018; Satpathy et al. 2019; Massara et al. 2021, 2023) or revert back to using one-point statistics (e.g. Bernardeau & Valageas 2000; Uhlemann et al. 2016, 2020; Barthelemy, Codis & Bernardeau 2021; Boyle et al. 2023; Marques et al. 2023).

On large scales, one of the most striking features of the matter distribution is the presence of the cosmic web (Gregory & Thompson 1978; Joeveer & Einasto 1978; J oeveer, Einasto & Tago 1978; Klypin & Shandarin 1983; Gott, Melott & Dickinson 1986; White et al. 1987; Vogeley et al. 1994b; Bond, Kofman & Pogosyan 1996), composed of voids (Zeldovich, Einasto & Shandarin 1982; Icke 1984; de Lapparent, Geller & Huchra 1986; Vogeley et al. 1994a), walls in between them (Zel'dovich 1970; Novikov 1975; Doroshkevich et al. 1980), separated by filaments (de Vaucouleurs 1953; Einasto, Joeveer & Saar 1980; Oort 1983; Dekel, West & Aarseth 1984) which finally intersect at cosmic nodes. This has sparked interest in

* E-mail: jshim@asiaa.sinica.edu.tw

building alternative probes informed by the topology of the cosmic web to measure cosmological parameters, such as the genus curve and Euler-Poincaré characteristic (e.g. Gott, Melott & Dickinson 1986; Melott et al. 1989; Mecke & Wagner 1991; Park & Gott 1991; Park, Gott & Choi 2001; James et al. 2009; Park & Kim 2010; Appleby et al. 2018a, 2021), Minkowski functionals (e.g. Mecke, Buchert & Wagner 1994; Schmalzing & Buchert 1997; Hikage et al. 2003; Natoli et al. 2010; Junaid & Pogosyan 2015; Appleby et al. 2018b; Goyal, Chingangbam & Appleby 2020; Appleby et al. 2022), percolation (e.g. Shandarin 1983; Yess, Shandarin & Fisher 1997; Shandarin & Yess 1998; Colombi, Pogosyan & Souradeep 2000; Zhang, Cheng & Chu 2018) and skeleton (e.g. Sousbie et al. 2008; Sousbie, Colombi & Pichon 2009; Sousbie, Pichon & Kawahara 2011), or persistent homology analysis (e.g. Sousbie, Pichon & Kawahara 2011; Pranav et al. 2017), alpha-shapes and Betti numbers (e.g. Van de Weygaert et al. 2011; Chingangbam et al. 2012; Park et al. 2013; Feldbrugge et al. 2019; Pranav et al. 2019).

Recently, it has been shown that the relative clustering of critical points of a density field is maintained nearly constant throughout the gravitational evolution (Shim et al. 2021, Appendix B), and can be measured accurately. Critical points are topological elements of a given field, and their attributes including position, height, curvature, and relative orientation encode the topological characteristics of the underlying field (Bond, Kofman & Pogosyan 1996; Pogosyan et al. 2009; Sousbie, Colombi & Pichon 2009; Gay, Pichon & Pogosyan 2012) and its evolution (Cadiou et al. 2020). One of their characteristic clustering features is that a pair of critical points with different curvatures and heights cannot be arbitrarily close. This exclusion zone, or the strong anticlustering region (Lumsden, Heavens & Peacock 1989; Mo & White 1996; Sheth & Lemson 1999; Baldauf et al. 2016; Shim et al. 2021), appears more evidently in the cross-correlations between critical points with the opposite-sign biases (Shim et al. 2021). Interestingly, Shim et al. (2021) showed that the sizes of the exclusion zones in the initial Gaussian field are fairly consistent with those measured at late time, suggesting that we have a theoretical handle on their cosmology dependence since the Gaussian expectation value can be derived from first principles. On the other hand, the amplitude of this exclusion zone is shown to depend on how smooth the underlying field is (Baldauf et al. 2016), indicating a cosmological dependence which we set forth to establish in this paper.

In expanding such exploration into cosmological tests, the redshift invariance of topology statistics emerges as a pivotal metric, as first introduced in Park & Kim (2010). Leveraging the conserved nature of the genus amplitude in density fields smoothed on large scales, these authors present a method to constrain the cosmological model. This involves identifying the correct expansion history of the Universe that minimizes the evolution of the genus amplitude with redshift. Aligning with this strategy, we introduce an approach utilizing the exclusion radius as a standard ruler to probe cosmology without delving into specific practicalities. We measure the size of the exclusion zone in critical point correlation functions and show how it can perform as a cosmological probe. Specifically, we focus on cross-correlations involving peak-wall, peak-void, filament-wall, and filament-void pairs – tracers that are oppositely biased to matter density fields. We rely on the suite of cosmological N -body simulations to measure the critical point statistics.

The outline of the paper is as follows: Section 2 describes briefly the multiverse simulation; Section 3 introduces estimators for the exclusion zone; Section 4 presents our results on the Ω_m -dependent variations of the exclusion zone radius, and on estimating w_{de} when different redshifts fields are considered, while Section 5 concludes.

Table 1. Summary of cosmological parameter values of five cosmologies considered. The second-row model is the fiducial cosmology.

| | Ω_m | w_{de} | Ω_{de} |
|--------------------------|------------|----------|---------------|
| (Ω_m^-, w_{de}^0) | 0.21 | −1.0 | 0.79 |
| (Ω_m^0, w_{de}^0) | 0.26 | −1.0 | 0.74 |
| (Ω_m^+, w_{de}^0) | 0.31 | −1.0 | 0.69 |
| (Ω_m^0, w_{de}^-) | 0.26 | −1.5 | 0.74 |
| (Ω_m^0, w_{de}^+) | 0.26 | −0.5 | 0.74 |

Appendix Section A shows the apparent evolution of the exclusion radius for a larger smoothing scale, while Section B discusses the theoretical expectation of the exclusion radius.

2 SIMULATION SET

In this paper, we rely on the multiverse simulations introduced in Park et al. (2019) and Tonegawa et al. (2020) which are a set of cosmological N -body simulations designed to test the effects of cosmological parameters on the clustering of cosmic structures. This set of five simulations varies the cosmological parameters centered on a fiducial Λ CDM cosmology with $\Omega_m = 0.26$, $\Omega_{de} = 0.74$, $H_0 = 72 \text{ km s}^{-1} \text{ Mpc}^{-1}$, and $w_{de} \equiv p_{de}/\rho_{de} = -1$, (in alignment with WMAP5 constraints; Dunkley et al. 2009). The initial displacement and velocity of the simulated dark matter particles are obtained by applying the second-order Lagrangian perturbation theory (Jenkins 2010). The same set of random numbers has been employed to produce the initial density perturbations across all simulations, enabling a more straightforward comparison between them without the confounding effects of cosmic variance. Specifically, two of these simulations involve an alteration in the matter density parameter by ± 0.05 relative to the fiducial model, maintaining the dark energy equation of state (EOS) at $w_{de} = -1$. The remaining two simulations, based on quintessence models (Sefusatti & Vernizzi 2011), introduce a deviation in w_{de} by ± 0.5 from the fiducial dark energy EOS, with Ω_m consistently set to 0.26. Cosmological parameters for the five cosmologies including the fiducial one are summarized in Table 1.

The power spectra are normalized such that the root mean square of the linearly evolved matter fluctuation at $z = 0$ yields a value of $\sigma_8 = 0.794$ when smoothed with a spherical top hat with $R_s = 8 h^{-1} \text{ Mpc}$. The number of particles in each simulation is 2048^3 and the comoving size of the simulation box is $1024 h^{-1} \text{ Mpc}$. The initial power spectrum at a redshift $z_{init} = 99$ was computed with the CAMB package. The N -body integrator is an extension of the original GOTPM code (Dubinski et al. 2004) which evolve particles according to the modified Poisson equation

$$\nabla^2 \phi = 4\pi G a^2 \bar{\rho}_m \delta_m \left(1 + \frac{D_{de}}{D_m} \frac{\Omega_{de}(a)}{\Omega_m(a)} \right), \quad (1)$$

where D_{de} and D_m are the linear growth factors of the dark energy and matter, respectively (see Sefusatti & Vernizzi 2011 for details).

3 EXCLUSION ZONE ESTIMATORS

Let us first briefly describe how we define and measure the size of the exclusion zones. We refer to Shim et al. (2021) for more details. The first step is to compute a smooth density field in real space at the relevant redshifts. Density fields are calculated on 512^3 grids by applying the Cloud-In-Cell method to the dark matter particle distribution. We then smooth these density fields with Gaussian kernel over 4 different smoothing scales $R_s = 16, 14, 10$, and

$6 h^{-1} \text{Mpc}$. Note that the smallest smoothing scale corresponds to a typical size of an average density region of mass-scale around $10^{15} M_{\odot}$.

3.1 Critical points

The critical points are defined as positions where the gradient of the dark matter density field vanishes (Milnor 1963; Bardeen et al. 1986; Shim et al. 2021). Based on the typical shape of isosurfaces in that neighborhood, the four types are labeled according to the sign of the Hessian's eigenvalues: peaks (\mathcal{P}) with signature $---$, voids (\mathcal{V}) with signature $+++$, filament-type saddles (\mathcal{F}) with signature $--+$, and wall-type saddles (\mathcal{W}) with signature $-++$. They are proxies for the geometry of the cosmic web (Bond, Kofman & Pogosyan 1996) of the underlying density field, tracing respectively clusters, voids, filaments, and walls (Pogosyan et al. 2009; Sousbie, Colombi & Pichon 2009) on a mass scale relevant to the adopted smoothing scale.

3.2 Finding critical points

The detection of critical points in a smoothed dark matter density field relies on a second-order Taylor-expansion of the density field near a critical point, \mathbf{x}_c :

$$\mathbf{x} - \mathbf{x}_c \approx (\nabla \nabla \rho)^{-1} \nabla \rho, \quad (2)$$

where ρ is the density field, $\nabla \rho$ the local gradient and $\nabla \nabla \rho$ the local hessian matrix. The detection algorithm proceeds as follows: (a) For each cell in the grid, compute $\nabla \rho$ and $\nabla \nabla \rho$, (b) solve equation (2) discarding solutions beyond a distance larger than one pixel, and (c) loop over cells that contain multiple critical points of the same kind, retaining for each only the critical point closest to the center of the cell (the technique was originally introduced by one of the authors for Colombi, Pogosyan & Souradeep 2000).

3.3 Computing clustering correlation functions

We count the pairs of critical points with rarity above or below a certain threshold to quantify their clustering characteristics. We define the rarity of critical points as

$$v \equiv \delta / \sigma, \quad \text{with } \delta \equiv \rho / \bar{\rho} - 1, \quad \text{and } \sigma^2 \equiv \langle \delta^2 \rangle, \quad (3)$$

where δ is the overdensity contrast of the smoothed density field, $\bar{\rho}$ the average density and σ is the root mean square fluctuation of the field.

For peak and filament (respectively void and wall) critical points, we identify points with rarity higher (respectively lower) than a given threshold. In this analysis, the rarities v_{type}^+ and v_{type}^- are chosen to trace the highest and lowest 20 per cent-rarity critical points, so that

$$N_{\text{type}}(v \geq v_{\text{type}}^+) = 0.2 N_{\text{type}}, \quad N_{\text{type}}(v \leq v_{\text{type}}^-) = 0.2 N_{\text{type}}, \quad (4)$$

respectively, for peaks and filaments, and for voids and walls. Here, $N_{\text{type}}(v \geq v_{\text{thresh}})$ represents the number of critical points of a given type above the threshold v_{thresh} (here 20 per cent rarest) while N_{type} is the total number of critical points of this type. As discussed in Shim et al. (2021), this choice is driven by our requirement to sample populations that represent the same abundance for a given type of critical point. We then measure cross-correlation functions with the estimator given by Davis & Peebles (1983)

$$1 + \xi_{ij}(r) = \frac{\langle C_i C_j \rangle}{\sqrt{\langle C_i R_j \rangle \langle C_j R_i \rangle}} \sqrt{\frac{N_{R_i} N_{R_j}}{N_{C_i} N_{C_j}}}, \quad (5)$$

where C_i refers to a particular catalogue $i \in \{\mathcal{P}, \mathcal{F}, \mathcal{W}, \mathcal{V}\}$ and R_i is a corresponding catalogue with randomly uniformly distributed points in the same volume. Here, $\langle XY \rangle$ represents the number counts of the pairs between X and Y separated by r . The size of the sample, N_{R_i} , of the random catalogue is a factor of 100 or larger than the size of our simulated data sets, N_{C_i} .

3.4 Defining exclusion radii

The exclusion zone size, denoted as R_{ex} , is measured from the cross-correlation functions. Specifically, this is achieved by identifying the minimum distance at which the cross-correlation deviates from $\xi = -1$. In practice, we identify the radius at which

$$1 + \xi(R_{\text{ex}}) = \epsilon, \quad (6)$$

with the deviation from perfect anticorrelation set at $\epsilon = 0.01$. We note that the exclusion radius for a particular density field depends on the choice of rarity levels of critical points and on the choice of ϵ that defines departure from perfect anticorrelation. Decreasing rarity levels tends to yield smaller exclusion radii, as the difference in height between critical points will decrease. Conversely, it should increase the number of critical point pairs, thereby providing more reliable estimates for the exclusion radius.

We estimate measurement uncertainties to evaluate the statistical significance of the impact of cosmological parameters on the exclusion radius. We divide the simulation box into eight separate, non-intersecting regions. For each sub-volume, we compute the cross-correlation function using critical points within that sub-volume. While doing this, we accounted for edge effects by creating a random sample within the same sub-volume. We then measure the exclusion radii from those cross-correlation functions. The measurement uncertainties are represented by the standard error of the mean, which is the standard deviation divided by the square root of the number of sub-volumes.

4 RESULTS

Let us now turn to our main results on matter density and dark energy equation of state estimation using exclusion zone measurements.

4.1 Exclusion radius and matter density parameter

We first explore how the exclusion radius varies with the matter density parameter. As illustrated in Fig. 1, we measure the cross-correlation functions between peak/filament and void/wall critical points across five different cosmologies. The cross-correlations reveal varying exclusion zones based on the combination of critical points. Notably, the filament-wall combination presents the smallest exclusion zone, while the peak-void combination showcases the largest. This observation aligns with the understanding that the exclusion zone expands with increasing differences in height and curvature, as shown in Baldauf et al. (2016) and Shim et al. (2021). After the emergence of the exclusion zone, cross-correlations start to deviate from $\xi = -1$ and become less anticlustered with increasing separation. Because peak/filament and void/wall points are oppositely biased tracers of the underlying matter density field, their cross-correlations are always negative, eventually approaching $\xi = 0$ as expected (Kaiser 1984) at separations larger than $r \approx 10R_{\xi}$.

Comparing cases for different matter density parameters reveals that the cross-correlations show a smaller exclusion radius for a larger matter density parameter. This implies that the exclusion radius

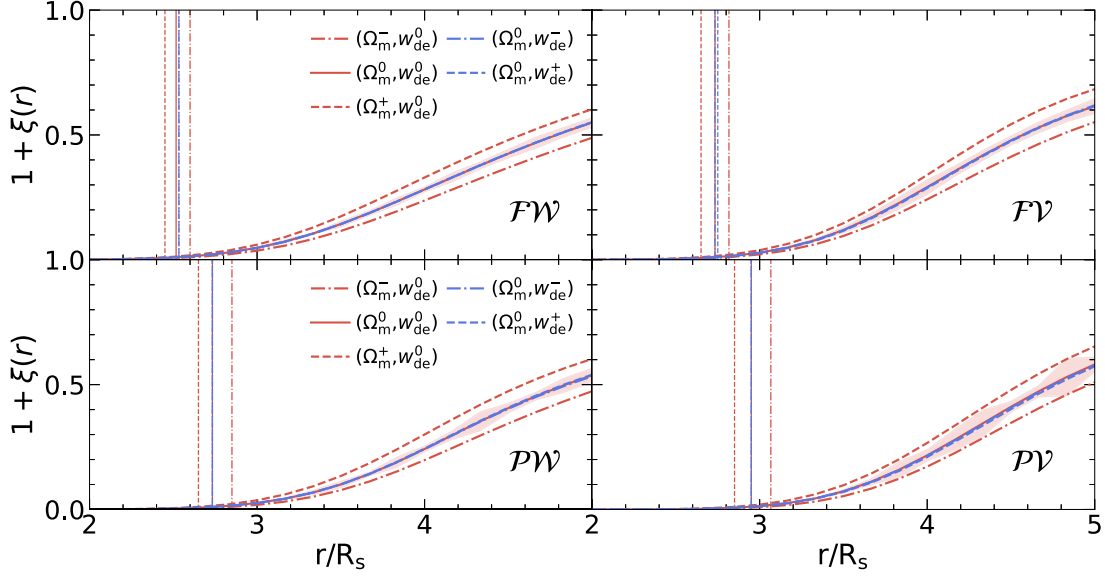


Figure 1. Two-point cross-correlation functions for pairs of positively and negatively biased critical points for the five different cosmologies as labeled. Correlation functions for the \mathcal{FW} , \mathcal{FV} , \mathcal{PV} , and \mathcal{PV} are shown clockwise from the upper-left panel. The adopted Gaussian smoothing scale R_s is $6 h^{-1}\text{Mpc}$. Vertical lines represent the exclusion zone radii and shaded regions show the standard errors around the fiducial cosmology. Note that the correlation function for the fiducial cosmology (solid) is nearly identical to those with the different equations of state dark energy models. However, the two-point correlation function depends on Ω_m , see Fig. 2.

is impacted by the matter density. In contrast, when focusing on dark energy models with non-standard dark energy EOS parameters w_{de} , their exclusion radii are very similar to the fiducial model. This suggests that changes to the dark energy parameter do not significantly affect the exclusion radius. Thus, the size of the exclusion zone is mainly dictated by the amount of matter and remains largely unaffected by variations in the dark energy EOS.

We now quantitatively compare the mean exclusion radii across five different cosmologies at lower redshifts, as illustrated in Fig. 2. The cross-correlations involving filaments and peaks are presented in the top and lower panels, respectively. Different shaded bars represent different redshift snapshot boxes for each cosmological parameter set. We observe a clear Ω_m -dependence of the exclusion radius. For instance, the exclusion zone shrinks as the matter density increases. However, adjusting the dark energy parameter shows a minimal impact on the exclusion radius. This is a consequence of the power spectrum slope at the scales of interest becoming shallower as Ω_m increases but remaining nearly invariant with w_{de} . We discuss the cosmological parameter dependence of the exclusion zone in detail below while relating it to the theoretical expectation for the distance between extrema. Finally, when focusing on the time evolution, the exclusion zone remains remarkably stable in the redshift ranges investigated.

In Fig. 3, we quantify how significant the difference in the exclusion radius of each cosmology is from the fiducial case. The significance \mathcal{S} is calculated as

$$\mathcal{S} \equiv \frac{R_{\text{ex}}^x - R_{\text{ex}}^{\text{fid}}}{\sqrt{\Sigma_x^2 + \Sigma_{\text{fid}}^2}}, \quad (7)$$

where R_{ex}^x and Σ_x represent the exclusion radius and standard error for a particular cosmology, while $R_{\text{ex}}^{\text{fid}}$ and Σ_{fid} are for the fiducial model. We find that the significance values tend to be larger for the filament-wall correlation compared to other critical point combinations. Conversely, the peak-void correlation shows the smallest significance. This trend of larger (smaller) significance values when

involving only saddles (extrema) arises from the differing numbers of critical points of each type. In a Gaussian random field, the ratio of saddle-to-extrema is approximately 3 (see e.g. Gay, Pichon & Pogosyan 2012; Shim et al. 2021). Consequently, the number of pairs for the filament-wall correlation is roughly an order of magnitude larger than that for the peak-void case. Therefore, the standard error is typically smaller for the case only involving saddles than extrema leading to a larger significance value for cross-correlations involving saddles. While the significance for one type of cross-correlation might not be sufficient to distinguish between different cosmologies, combining results from all four distinct measurements will enhance the overall constraining power.

We identify critical points on a particular scale determined by the smoothing length adopted, so next we examine how the exclusion radius changes with the smoothing scale, as this allows us to probe the clustering of critical points corresponding to a different mass scale. Fig. 4 illustrates the variation of the exclusion radius measured from the matter density field smoothed on different smoothing scales. We observe a common trend that the rescaled exclusion radius decreases with the smoothing scale. This is evident across different cosmologies and types of cross-correlations considered. We consistently confirm that the exclusion radius shows a distinct dependence on the matter density on different smoothing scales. For instance, the rescaled R_{ex} is always larger at all smoothing scales investigated for a cosmology with a smaller matter density. On the other hand, when varying the dark energy EOS parameters, the exclusion radii are remarkably consistent with the fiducial case.

Interestingly, we find that the behaviour of R_{ex}/R_s seen in Fig. 4 is similar to the prediction for R_*/R_s as depicted in Fig. B2, which leads us to examine the relation between them. Here, R_* represents the typical separation between extrema points and is defined by

$$R_* = \frac{\sigma_1}{\sigma_2}. \quad (8)$$

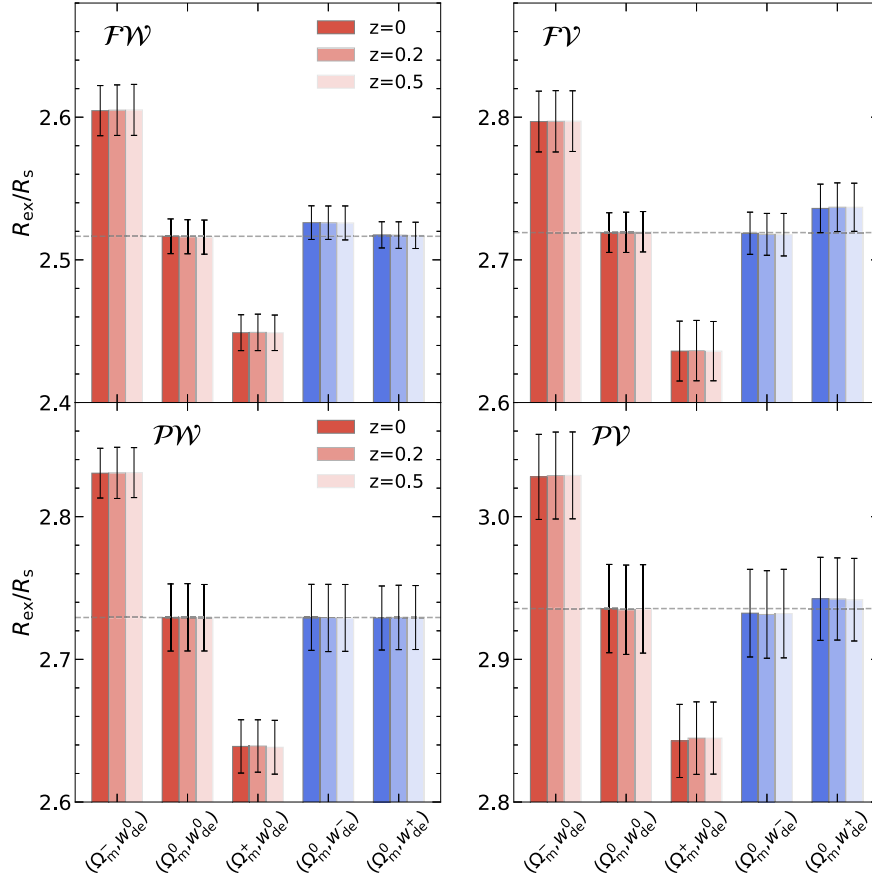


Figure 2. Exclusion zone radius averaged over 8 measurements from the simulations for the five different cosmologies. We normalized the exclusion zone radius by the smoothing scale R_s adopted since R_{ex} linearly depends on the smoothing scale. Error bars represent the standard errors of the mean. The grey horizontal line marks the exclusion zone radius for the fiducial cosmology with $\Omega_m = 0.26$ and $w_{\text{de}} = -1$. For this plot, we adopt the Gaussian smoothing scale $R_s = 6 h^{-1}\text{Mpc}$. The trend of the exclusion radius with Ω_m is consistent with the scaling involving n_s in equation (11) if one associates R_{ex} with R_* , see the text for details.

The moments of the smoothed power spectrum are calculated as

$$\sigma_i^2(R_s) \equiv \frac{1}{2\pi^2} \int_0^\infty dk k^2 P(k) k^{2i} W^2(k R_s), \quad (9)$$

where we adopt the Gaussian smoothing kernel,

$$W(k R_s) = \exp\left(-\frac{1}{2} k^2 R_s^2\right), \quad (10)$$

which serves as a low-pass filter suppressing power on scales below $1/R_s$ for the power spectrum $P(k)$ weighted by varying powers of k^{2i} . As depicted in Fig. B3, we find a linear scaling relation between R_{ex} and R_* . Associating these two provides a way to connect the measurements of exclusion radius to theoretical predictions based on Gaussian random fields. Indeed, for a Gaussian random field with (locally) scale-invariant power spectra, $P(k) \propto k^{n_s}$, the rescaled typical distance between extrema,

$$\frac{R_*}{R_s} = \sqrt{\frac{2}{n_s + 5}} \quad (11)$$

is solely determined by the effective power-law index of the power spectrum, $n_s[k = 1/R_s]$. The effective slope is itself sensitive to the chosen smoothing scale, R_s , and to the matter density, Ω_m , as displayed in Fig. B1, bottom panel. Now, we can understand how the rescaled R_* varies with respective matter density, dark energy EOS, and smoothing scale. Since the power spectrum slope either

increases when the smoothing scale or matter density parameter becomes larger (see Fig. B1), and hence, according to the equation (11) the rescaled R_* will decrease with the smoothing scale and matter density. On the other hand, R_*/R_s does not vary with the dark energy EOS since it has no impact on the power spectrum slope. Consequently, when relying on the linear relation between R_{ex} and R_* (see Fig. B3) the observed behaviours of R_{ex} depicted in Figs 2 and 4 can be qualitatively explained with the prediction made for R_* based on Gaussian random fields.

4.2 Exclusion radius and dark energy EOS

Let us now describe how we can extract information on the dark energy parameter using the exclusion radius, even though the effect of dark energy on the measured exclusion radius is shown to be negligible. Our strategy is based on the redshift invariance of the exclusion radius in comoving space.

We follow the approach presented in Park & Kim (2010), Blake, James & Poole (2014), and Appleby et al. (2018a), where matter density and dark energy parameters were constrained to minimize the apparent redshift evolution of the genus of the underlying matter density field.

Let us recall the strategy. It relies on the fact that the redshift invariance of the measured genus amplitude is achieved only when

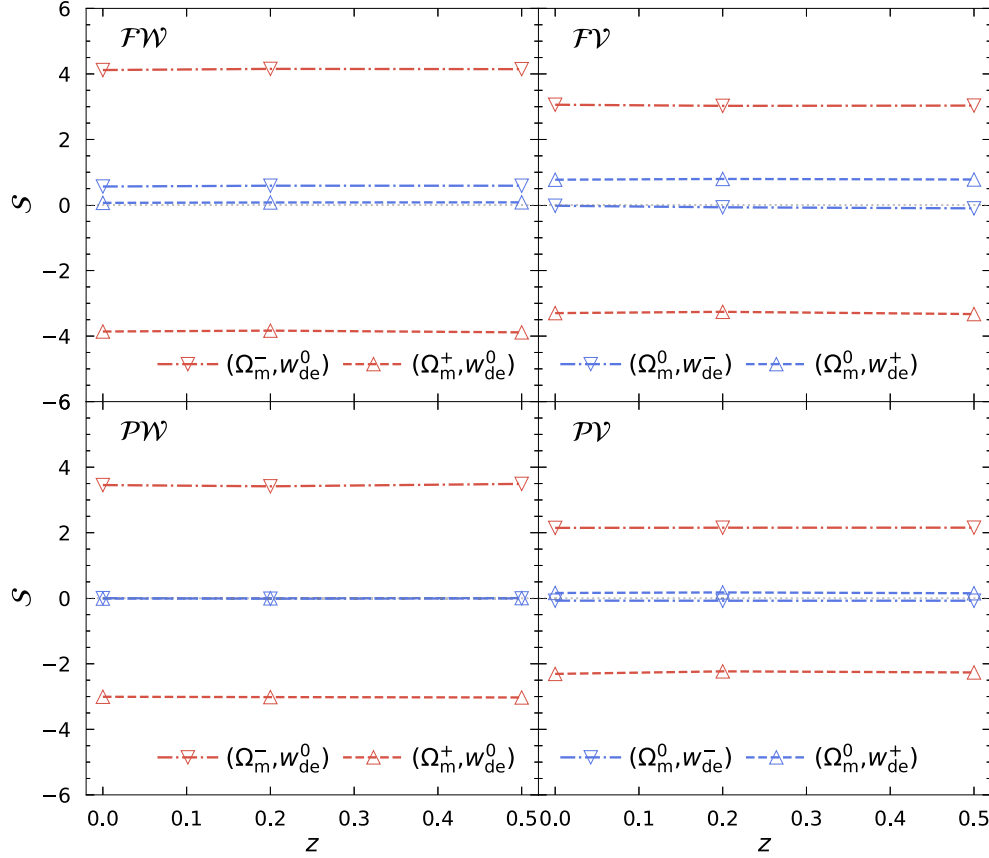


Figure 3. Significance, S , of the difference in the exclusion radius from the fiducial cosmology as a function of redshift. For this plot, we adopt the Gaussian smoothing scale $R_s = 6 h^{-1} \text{Mpc}$. Note that we allow the significance to have both signs as they can indicate the direction of the difference from the fiducial case.

the adopted cosmology for the redshift–distance relation matches the underlying true cosmology. Indeed, the genus amplitude, \mathcal{A} , obeys

$$\mathcal{A} \propto ((k^2))^{3/2} \propto \frac{1}{R_0^3}, \quad (12)$$

where $R_0 \equiv \sigma_0/\sigma_1$ characterizes the typical separation between zero crossing of a density field. Hence \mathcal{A} is expressed in terms of the ratio of moments defined by equation (9). Again, for scale-invariant power-spectra, the genus amplitude \mathcal{A} only depends on the effective power index, n_s , as $\text{red}(\sqrt{2/(n_s + 3)})^3$. Since the slope of a power spectrum changes with R_s (because the power spectrum is not scale invariant on the scales we are considering, the lower panel of Fig. B1), if an incorrect cosmology is assumed, the adopted smoothing scale effectively corresponds to a different length-scale, hence \mathcal{A} is altered.¹

Similarly and importantly, if the wrong cosmology is adopted, we also expect to observe an apparent redshift evolution of R_{ex} because it is linearly related to R_* (as described in Appendix B). We highlight that the measurements of exclusion radii in the evolved matter density field, which has deviated from its initial Gaussian nature, well align with the predictions made in the Gaussian random field for R_* . Therefore, in theory, it is indeed possible to estimate the deviation of the exclusion radius from the reference point as a function of redshift by calculating the effective smoothing scale for an adopted cosmological model.

In Fig. 5, we show how the exclusion radius for a trial cosmology deviates from the fiducial case as a function of redshift. We observe a redshift evolution of the exclusion radius when the trial cosmology is inconsistent with the true underlying cosmology. For example, the exclusion radius monotonically grows with redshift when the matter density and dark energy parameters are larger than the true values, whereas it becomes smaller at higher redshifts in cosmologies with smaller matter density and dark energy parameters. We observe a larger departure from the reference for non-fiducial dark energy models. This reflects the fact that, at low z , the distance estimates are more strongly impacted by dark energy than matter density, in the redshift range of interest. Thus, the evolution of the apparent exclusion radius is more sensitive to the properties of dark energy.

We then calculate the potential measurement errors for an all-sky survey up to various redshifts to assess if it is possible to detect such redshift evolution of the exclusion radius given those survey volumes. We base our error estimates on the standard error achieved from the simulation volume $V_{\text{sim}} = 1 h^{-3} \text{Gpc}^3$. Let us assume that these errors reduce by $\sqrt{V_{\text{sim}}/V_{\text{sur}}}$, similar to the behaviour of shot-noise, where V_{sur} is survey volume. For a survey with $V_{\text{sur}} \approx 2.5 h^{-3} \text{Gpc}^3$, scanning up to $z = 0.3$, the departure of w_{de} -shifted dark energy models from the fiducial cosmology can be detected approximately at 1.5σ significance level. When a survey extends to $z = 0.5$ reaching $V_{\text{sur}} \approx 10 h^{-3} \text{Gpc}^3$, the detection significances for the non-fiducial dark energy models can increase approximately to 3.8σ , while those for Ω_m -shifted models eventually become marginal. We expect that one can more significantly detect the redshift variation of the exclusion radius when measuring it at

¹ In fact, genus-based estimators are more sensitive to slope changes near $n_s = -1$ because $R_0 \propto 1/\sqrt{n_s + 3}$, whereas $R_* \propto 1/\sqrt{n_s + 5}$.

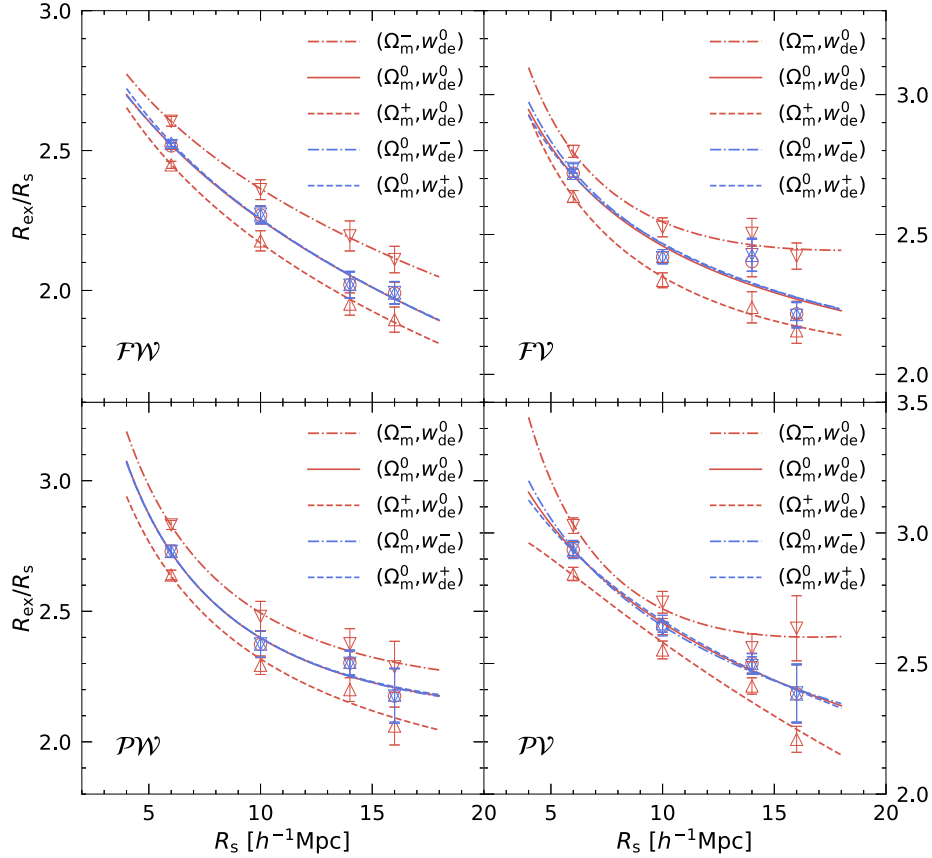


Figure 4. Measured exclusion zone radius as a function of smoothing scale for four different types of cross-correlations. Correlation functions for \mathcal{FW} , \mathcal{FV} , \mathcal{PV} , and \mathcal{VW} are shown clockwise from the upper-left panel. The symbols and lines represent the measured exclusion radius and best fit to these measurements, respectively. Error bars are measured as the standard error of the mean. Again the trend is consistent with theoretical expectation if one associates R_{ex} to R_* , as confirmed to the first order in Fig. B3.

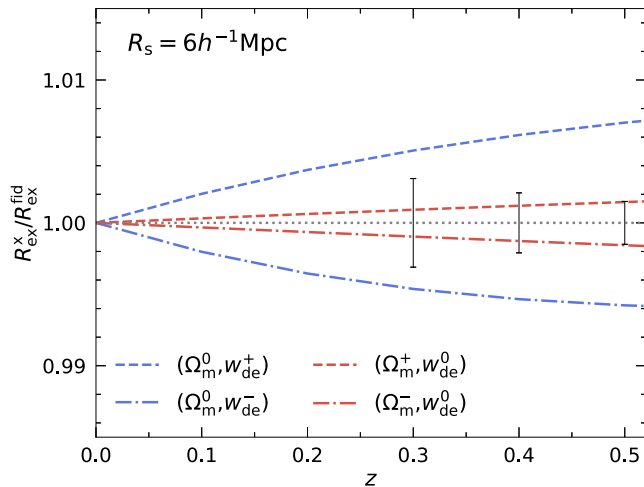


Figure 5. Expected redshift evolution of R_{ex} relative to the true value when adopting trial cosmologies with different Ω_m or w_{de} for the redshift–distance relation. The exclusion radius for the true underlying cosmology is shown in a grey dotted line and vertical error bars at redshifts $z = 0.3, 0.4,$ and 0.5 represent the estimated measurement uncertainties about the fiducial values, given the volumes surveyed up to those respective redshifts. Note that the true exclusion radius does not evolve with redshift.

higher redshifts. This is partly because the predicted amplitude of redshift variation gradually grows with redshift. In addition, even with a relatively narrow redshift span, the volume scanned through a non-full-sky survey targeting higher redshifts can be larger than the largest comoving volume considered here, for instance, $V_{\text{sur}} = 10 h^{-3} \text{Gpc}^3$ up to $z \approx 0.5$. Therefore, a higher significance detection should be available from surveys aiming at high redshifts. Note that we can also combine the exclusion radius measurements using four distinct types of cross-correlations, which should yield more robust measurements (although these measurements from the same density field are not strictly independent). For completeness, we also show the expected redshift evolution of the exclusion radius for $R_s = 16 h^{-1} \text{Mpc}$ with the same mock surveys in Fig. A1. As expected, the error bars are larger.

5 CONCLUSIONS & PERSPECTIVES

This paper advocates that the exclusion radii, R_{ex} , define standard rulers on multiple scales: on linear scales, they can be computed using Lagrangian theory (Bardeen et al. 1986; Shim et al. 2021), while on smaller non-linear scales they can be extracted from cosmological simulations, as was done in this paper. The value of R_{ex} mainly constrains Ω_m (Fig. 3) and may also be potentially used for measuring n_s as can be done with the genus amplitude analysis (Appleby et al. 2020). Our results support that, at a given physical scale, the exclusion radius is redshift-invariant at first order, which

can be leveraged to constrain the equation of state of dark energy w_{de} (Fig. 5). More precise results could be obtained by calibrating the scale-dependence and redshift evolution of the relation on N -body simulations. We find that the redshift evolution and cosmology dependence of R_{ex} can be remarkably captured using the locally scale-invariant quantity R_* , which we can predict from linear theory. This implies that the topology we measure at late time is already imprinted in the Gaussian initial state, and is not destroyed by gravitational collapse. Thus, the non-Gaussian final state mostly preserves its Gaussian initial topology. We carried out a naive error budget and found that the accuracy of the parameter estimation corresponds to a 4σ detection of a change in matter content of 5 per cent in $1 h^{-3}\text{Gpc}^3$, or roughly at 3.8σ detection of 50 per cent change in the dark energy parameter using a full sky survey up to redshift 0.5. These numbers could be improved by performing a joint analysis of all exclusion radii, accounting for the fact that they are not independent, or by exploring jointly different rarity thresholds.

At this stage, we assumed that the linear relation between R_{ex} and R_* given in Appendix B holds for the range of redshifts considered; investigating its redshift dependence is of interest as it would allow us to mitigate its residual effect (beyond the linear scaling shown in Fig. B3) on smaller scales, but is beyond the scope of the current analysis. Conversely, extending this investigation to higher redshift would clearly be of interest given the depth of upcoming surveys², and is also postponed to later work.

The accuracy of these standard rulers was assessed here using the multiverse set of simulations in a fairly idealized setting. Our goal was to demonstrate the potential to build such rulers out of the two-point correlation functions of critical points, setting aside complications from completeness issues, tracer biases, SNR, and redshift space distortions. The companion paper, Kraljic et al. (2022), investigated how Lyman α tomography can, in the context of the WEAVE mission (Dalton et al. 2012; Pieri et al. 2016), open access to the clustering of critical points and the possibility of exclusion zone estimation. While the focus of this paper was on exclusion zones, Kraljic et al. (2022) showed that the position of the maxima of the cross-correlations of critical points of the same sign could also be estimated from tomography. Combining both approaches could potentially allow even tighter constraints to be set on cosmological parameters. While more realistic, Kraljic et al. (2022) still only involved mock data, and should of course be revisited with other tomographic 3D surveys such as PFS (Takada et al. 2014), MOSAIC on ELT (Puech et al. 2018), MSE (The MSE Science Team et al. 2019), but also with spectroscopic or photometric redshifts galactic surveys, such as Euclid (Laureijs et al. 2011), DESI (DESI Collaboration 2016), PFS, WFIRST (Roman Space Telescope; Spergel et al. 2013), or LSST (Rubin Observatory; Ivezić et al. 2019).

The cosmology dependence of the clustering of critical point should also be investigated in 2D maps such as weak lensing maps (Laureijs et al. 2011; Hildebrandt et al. 2017), line intensity maps (CHIME Collaboration et al. 2022), and photometric redshift surveys (Doré et al. 2014).

It would finally be of interest to compute the autocorrelation function of saddle points in redshift space, which are less subject to finger of god effects given the density they probe. This would allow for a more robust Alcock–Paczynski test (Alcock & Paczynski 1979), as one would expect that the overall motion of the local cosmic web does not impact such correlations.

²Euclid, LSST, WFIRST, SphereX, WEAVE, MSE, PFS, to name a few.

ACKNOWLEDGEMENTS

We thank an anonymous referee for helpful comments that helped improve the original manuscript. We thank C. Laigle for insightful conversations. We also thank the Kavli Institute for Theoretical Physics for hosting the workshop ‘CosmicWeb23: connecting Galaxies to Cosmology at High and Low Redshift’ during which this project was advanced. This research was supported in part by grant National Science Foundation PHY-1748958 to the Kavli Institute for Theoretical Physics. JS is supported by Academia Sinica Institute of Astronomy and Astrophysics, and thanks the Korea Institute for Advanced Study for its hospitality when this paper was completed. SA is supported by an appointment to the Junior Research Group (JRG) Program at the Asia Pacific Center for Theoretical Physics through the Science and Technology Promotion Fund and Lottery Fund of the Korean Government, and was also supported by the Korean Local Governments in Gyeongsangbuk-do Province and Pohang City. JK was supported by a (0:funding-source 3:href="http://dx.doi.org/10.13039/501100024023")Korea Institute for Advanced Study/(0:funding-source) Individual Grant (KG039603) via the Center for Advanced Computation at Korea Institute for Advanced Study. We thank the Korea Institute for Advanced Study for providing computing resources (KIAS Center for Advanced Computation Linux Cluster System).

DATA AVAILABILITY

The data underlying this article will be shared on reasonable request to the corresponding author.

REFERENCES

- Alam S. et al., 2021, *Phys. Rev. D*, 103, 083533
 Alcock C., Paczynski B., 1979, *Nature*, 281, 358
 Appleby S., Park C., Hong S. E., Kim J., 2018a, *ApJ*, 853, 17
 Appleby S., Chingangbam P., Park C., Hong S. E., Kim J., Ganesan V., 2018b, *ApJ*, 858, 87
 Appleby S., Park C., Hong S. E., Hwang H. S., Kim J., 2020, *ApJ*, 896, 145
 Appleby S., Park C., Hong S. E., Hwang H. S., Kim J., Tonegawa M., 2021, *ApJ*, 907, 75
 Appleby S., Park C., Pranav P., Hong S. E., Hwang H. S., Kim J., Buchert T., 2022, *ApJ*, 928, 108
 Armijo J., Cai Y.-C., Padilla N., Li B., Peacock J. A., 2018, *MNRAS*, 478, 3627
 Baldauf T., Codis S., Desjacques V., Pichon C., 2016, *MNRAS*, 456, 3985
 Bardeen J. M., Bond J. R., Kaiser N., Szalay A. S., 1986, *ApJ*, 304, 15
 Barthelemy A., Codis S., Bernardeau F., 2021, *MNRAS*, 503, 5204
 Bernardeau F., 1994, *ApJ*, 433, 1
 Bernardeau F., Valageas P., 2000, *A&A*, 364, 1
 Beutler F. et al., 2011, *MNRAS*, 416, 3017
 Beutler F. et al., 2017, *MNRAS*, 466, 2242
 Blake C. et al., 2011, *MNRAS*, 418, 1725
 Blake C., James J. B., Poole G. B., 2014, *MNRAS*, 437, 2488
 Bond J. R., Kofman L., Pogosyan D., 1996, *Nature*, 380, 603
 Bouchet F. R., Strauss M. A., Davis M., Fisher K. B., Yahil A., Huchra J. P., 1993, *ApJ*, 417, 36
 Boyle A., Barthelemy A., Codis S., Habib S., Uhlemann C., Friedrich O., 2023, *Open J. Astrophys.*, 6, 22
 CHIME Collaboration, 2022, *ApJS*, 261, 29
 Cadiou C., Pichon C., Codis S., Musso M., Pogosyan D., Dubois Y., Cardoso J. F., Prunet S., 2020, *MNRAS*, 496, 4787
 Cappi A. et al., 2015, *A&A*, 579, A70
 Chingangbam P., Park C., Yogendran K. P., van de Weygaert R., 2012, *ApJ*, 755, 122
 Colombi S., Pogosyan D., Souradeep T., 2000, *Phys. Rev. Lett.*, 85, 5515
 Croton D. J. et al., 2004, *MNRAS*, 352, 1232
 Da Angela J., Outram P. J., Shanks T., 2005, *MNRAS*, 361, 879

- Dalton G. et al., 2012, in McLean I. S., Ramsay S. K., Takami H.eds, Proc. SPIE Conf. Ser. Vol. 8446, Ground-based and Airborne Instrumentation for Astronomy IV. SPIE, Bellingham, p. 84460P
- Davis M., Peebles P. J. E., 1983, *ApJ*, 267, 465
- Dawson K. S. et al., 2013, *AJ*, 145, 10
- de Lapparent V., Geller M. J., Huchra J. P., 1986, *ApJ*, 302, L1
- de Vaucouleurs G., 1953, *AJ*, 58, 30
- DESI Collaboration, 2016, preprint (arXiv:1611.00036)
- Dekel A., West M. J., Aarseth S. J., 1984, *ApJ*, 279, 1
- Dong F., Park C., Hong S. E., Kim J., Hwang H. S., Park H., Appleby S., 2023, *ApJ*, 953, 98
- Doré O. et al., 2014, preprint (arXiv:1412.4872)
- Doroshkevich A. G., Kotok E. V., Poliudov A. N., Shandarin S. F., Sigov I. S., Novikov I. D., 1980, *MNRAS*, 192, 321
- Dubinski J., Kim J., Park C., Humble R., 2004, *New Astron.*, 9, 111
- Dunkley J. et al., 2009, *ApJS*, 180, 306
- Einasto J., Joeveer M., Saar E., 1980, *MNRAS*, 193, 353
- Eisenstein D. J. et al., 2005, *ApJ*, 633, 560
- Feldbrugge J., van Engelen M., van de Weygaert R., Pranav P., Vegter G., 2019, *J. Cosmol. Astropart. Phys.*, 2019, 052
- Fry J. N., 1985, *ApJ*, 289, 10
- Gay C., Pichon C., Pogosyan D., 2012, *Phys. Rev. D*, 85, 023011
- Gott J. Richard III, Melott A. L., Dickinson M., 1986, *ApJ*, 306, 341
- Goyal P., Chingangbam P., Appleby S., 2020, *J. Cosmol. Astropart. Phys.*, 2020, 020
- Gregory S. A., Thompson L. A., 1978, *ApJ*, 222, 784
- Hikage C. et al., 2003, *PASJ*, 55, 911
- Hildebrandt H. et al., 2017, *MNRAS*, 465, 1454
- Hinshaw G., Banday A. J., Bennett C. L., Gorski K. M., Kogut A., 1995, *ApJ*, 446, L67
- Hou J., Slepian Z., Cahn R. N., 2023, *MNRAS*, 522, 5701
- Icke V., 1984, *MNRAS*, 206, 1P
- Ivezić Ž. et al., 2019, *ApJ*, 873, 111
- Jõeveer M., Einasto J., Tago E., 1978, *MNRAS*, 185, 357
- James J. B., Colless M., Lewis G. F., Peacock J. A., 2009, *MNRAS*, 394, 454
- Jenkins A., 2010, *MNRAS*, 403, 1859
- Joeveer M., Einasto J., 1978, in Longair M. S., Einasto J.eds, Proc. IAU Symp. Vol. 79, Large Scale Structures in the Universe. Kluwer, Dordrecht, p. 241
- Junaid M., Pogosyan D., 2015, *Phys. Rev. D*, 92, 043505
- Kaiser N., 1984, *ApJ*, 284, L9
- Klypin A. A., Shandarin S. F., 1983, *MNRAS*, 204, 891
- Kraljic K. et al., 2022, *MNRAS*, 514, 1359
- Laureijs R. et al., 2011, preprint (arXiv:1110.3193)
- Li X.-D., Park C., Sabiu C. G., Park H., Weinberg D. H., Schneider D. P., Kim J., Hong S. E., 2016, *ApJ*, 832, 103
- Li X.-D. et al., 2018, *ApJ*, 856, 88
- Lumsden S. L., Heavens A. F., Peacock J. A., 1989, *MNRAS*, 238, 293
- Marín F. A. et al., 2013, *MNRAS*, 432, 2654
- Marinoni C., Buzzzi A., 2010, *Nature*, 468, 539
- Marques G. A. et al., 2023, preprint (arXiv:2308.10866)
- Massara E., Villaescusa-Navarro F., Ho S., Dalal N., Spergel D. N., 2021, *Phys. Rev. Lett.*, 126, 011301
- Massara E. et al., 2023, *ApJ*, 951, 70
- Mecke K. R., Wagner H., 1991, *J. Stat. Phys.*, 64, 843
- Mecke K. R., Buchert T., Wagner H., 1994, *A&A*, 288, 697
- Melott A. L., Cohen A. P., Hamilton A. J. S., Gott J. Richard I., Weinberg D. H., 1989, *ApJ*, 345, 618
- Milnor J., 1963, Morse Theory. Princeton University Press, Princeton, N.J
- Mo H. J., White S. D. M., 1996, *MNRAS*, 282, 347
- Natoli P. et al., 2010, *MNRAS*, 408, 1658
- Neveux R. et al., 2020, *MNRAS*, 499, 210
- Nichol R. C. et al., 2006, *MNRAS*, 368, 1507
- Novikov I. D., 1975, *AZh*, 52, 1038
- Okumura T., Matsubara T., Eisenstein D. J., Kayo I., Hikage C., Szalay A. S., Schneider D. P., 2008, *ApJ*, 676, 889
- Okumura T. et al., 2016, *PASJ*, 68, 38
- Oort J. H., 1983, *ARA&A*, 21, 373
- Park C., Gott J. R. I., 1991, *ApJ*, 378, 457
- Park C., Kim Y.-R., 2010, *ApJ*, 715, L185
- Park C., Gott J. Richard, III, Choi Y. J., 2001, *ApJ*, 553, 33
- Park C. et al., 2013, *J. Korean Astron. Soc.*, 46, 125
- Park H., Park C., Sabiu C. G., Li X.-d., Hong S. E., Kim J., Tonegawa M., Zheng Y., 2019, *ApJ*, 881, 146
- Peebles P. J. E., Groth E. J., 1975, *ApJ*, 196, 1
- Percival W. J., Cole S., Eisenstein D. J., Nichol R. C., Peacock J. A., Pope A. C., Szalay A. S., 2007, *MNRAS*, 381, 1053
- Philcox O. H. E., 2022, *Phys. Rev. D*, 106, 063501
- Philcox O. H. E., Hou J., Slepian Z., 2021, preprint (arXiv:2108.01670)
- Pieri M. M. et al., 2016, in Reylé C., Richard J., Cambrésy L., Deleuil M., Pécontal E., Tresse L., Vauglin I.eds, SF2A-2016: Proceedings of the Annual Meeting of the French Society of Astronomy and Astrophysics. p. 259
- Pogosyan D., Pichon C., Gay C., Prunet S., Cardoso J. F., Sousbie T., Colombi S., 2009, *MNRAS*, 396, 635
- Pranav P., Edelsbrunner H., van de Weygaert R., Vegter G., Kerber M., Jones B. J. T., Wintraecken M., 2017, *MNRAS*, 465, 4281
- Pranav P. et al., 2019, *MNRAS*, 485, 4167
- Puech M. et al., 2018, in Evans C. J., Simard L., Takami H.eds, Proc. SPIE Conf. Ser. Vol. 10702, Ground-based and Airborne Instrumentation for Astronomy VII. SPIE, Bellingham, p. 107028R
- Sabiu C. G., Hoyle B., Kim J., Li X.-D., 2019, *ApJS*, 242, 29
- Satpathy S., A C Croft R., Ho S., Li B., 2019, *MNRAS*, 484, 2148
- Schmalzing J., Buchert T., 1997, *ApJ*, 482, L1
- Sefusatti E., Vernizzi F., 2011, *J. Cosmol. Astropart. Phys.*, 2011, 047
- Shandarin S. F., 1983, *Sov. Astron. Lett.*, 9, 104
- Shandarin S. F., Yess C., 1998, *ApJ*, 505, 12
- Sheth R. K., Lemson G., 1999, *MNRAS*, 304, 767
- Shim J., Codis S., Pichon C., Pogosyan D., Cadiou C., 2021, *MNRAS*, 502, 3885
- Slepian Z. et al., 2017, *MNRAS*, 469, 1738
- Sousbie T., Pichon C., Colombi S., Novikov D., Pogosyan D., 2008, *MNRAS*, 383, 1655
- Sousbie T., Colombi S., Pichon C., 2009, *MNRAS*, 393, 457
- Sousbie T., Pichon C., Kawahara H., 2011, *MNRAS*, 414, 384
- Spergel D. et al., 2013, preprint (arXiv:1305.5422)
- Sugiyama N. S. et al., 2023, *MNRAS*, 524, 1651
- Takada M. et al., 2014, *PASJ*, 66, R1
- The MSE Science Team, 2019, preprint (arXiv:1904.04907)
- Tonegawa M., Park C., Zheng Y., Park H., Hong S. E., Hwang H. S., Kim J., 2020, *ApJ*, 897, 17
- Uhlemann C., Codis S., Pichon C., Bernardeau F., Reimberg P., 2016, *MNRAS*, 460, 1529
- Uhlemann C., Codis S., Kim J., Pichon C., Bernardeau F., Pogosyan D., Park C., L'Huillier B., 2017, *MNRAS*, 466, 2067
- Uhlemann C., Friedrich O., Villaescusa-Navarro F., Banerjee A., Codis S., 2020, *MNRAS*, 495, 4006
- Van de Weygaert R. et al., 2011, preprint (arXiv:1110.5528)
- Vogeley M. S., Geller M. J., Park C., Huchra J. P., 1994a, *AJ*, 108, 745
- Vogeley M. S., Park C., Geller M. J., Huchra J. P., Gott J., Richard I., 1994b, *ApJ*, 420, 525
- White M., Padmanabhan N., 2009, *MNRAS*, 395, 2381
- White S. D. M., Frenk C. S., Davis M., Efstathiou G., 1987, *ApJ*, 313, 505
- Xu K., Jing Y. P., Zhao G.-B., Cuesta A. J., 2023, *Nat. Astron.*, 7, 1259
- Yess C., Shandarin S. F., Fisher K. B., 1997, *ApJ*, 474, 553
- Zel'dovich Y. B., 1970, *A&A*, 5, 84
- Zeldovich I. B., Einasto J., Shandarin S. F., 1982, *Nature*, 300, 407
- Zhang J., Cheng D., Chu M.-C., 2018, *Phys. Rev. D*, 97, 023534
- Zhang X., Huang Q.-G., Li X.-D., 2019, *MNRAS*, 483, 1655

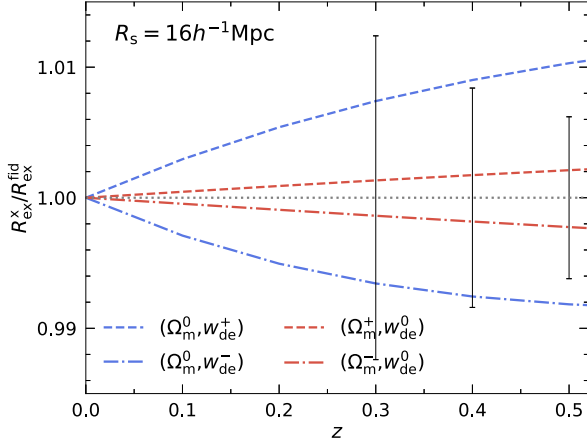


Figure A1. Same as Fig. 5 but for a smoothing scale $R_s = 16 h^{-1} \text{Mpc}$. Note that the deviation and measurement errors increase with smoothing scale. For example, the deviation and error are larger by factors of 1.4 and 3.5 for $(\Omega_m^0, w_{\text{de}}^+)$ cosmology (blue dashed) at $z = 0.5$.

APPENDIX A: PROBING DARK ENERGY EOS ON LARGER SCALES

Fig. A1 reproduces Fig. 5 for a different smoothing scale, $R_s = 16 h^{-1} \text{Mpc}$. As expected, as the number of critical points decreases the error bars for measuring w_{de} increases comparatively.

APPENDIX B: SCALING RELATIONS

Let us first describe how the shape of the matter power spectrum depends on cosmological parameters. Subsequently, we will elucidate the relation between R_{ex} and R_* in various cosmological models.

The linear matter power spectra for the cosmologies considered are depicted in Fig. B1. Primarily, the shape of the matter power spectrum varies with Ω_m , while its dependence on the dark energy equation of state w_{de} is minimal. The Ω_m -dependence of the power spectrum is attributed to the shift in the scale of matter–radiation equality as the matter density parameter changes.

In Fig. B2, we present the moment ratio R_* as a function of the smoothing scale R_s , based on the matter power spectra shown in Fig. B1. The normalized R_* decreases either with increasing smoothing scale or larger matter density. However, changing the dark energy EOS exhibits a minimal impact on R_* . As R_* probes

Table B1. Slope, a_1 , and intercept, a_2 , of the linear scaling relations between R_{ex} and R_* for \mathcal{FW} , \mathcal{FV} , \mathcal{PW} , and \mathcal{PV} for the cosmologies considered.

| Cosmology | | \mathcal{FW} | \mathcal{FV} | \mathcal{PW} | \mathcal{PV} |
|---------------------------------|-------|----------------|----------------|----------------|----------------|
| $(\Omega_m^-, w_{\text{de}}^0)$ | a_1 | 2.54 | 3.12 | 2.77 | 3.27 |
| | a_2 | 3.53 | 1.49 | 3.49 | 2.06 |
| $(\Omega_m^0, w_{\text{de}}^0)$ | a_1 | 2.35 | 2.85 | 2.70 | 2.97 |
| | a_2 | 4.20 | 2.79 | 3.46 | 3.63 |
| $(\Omega_m^+, w_{\text{de}}^0)$ | a_1 | 2.26 | 2.76 | 2.57 | 2.76 |
| | a_2 | 4.38 | 2.87 | 3.85 | 4.54 |
| $(\Omega_m^0, w_{\text{de}}^-)$ | a_1 | 2.35 | 2.85 | 2.70 | 2.97 |
| | a_2 | 4.21 | 2.88 | 3.48 | 3.64 |
| $(\Omega_m^0, w_{\text{de}}^+)$ | a_1 | 2.34 | 2.87 | 2.71 | 2.97 |
| | a_2 | 4.28 | 2.73 | 3.42 | 3.67 |

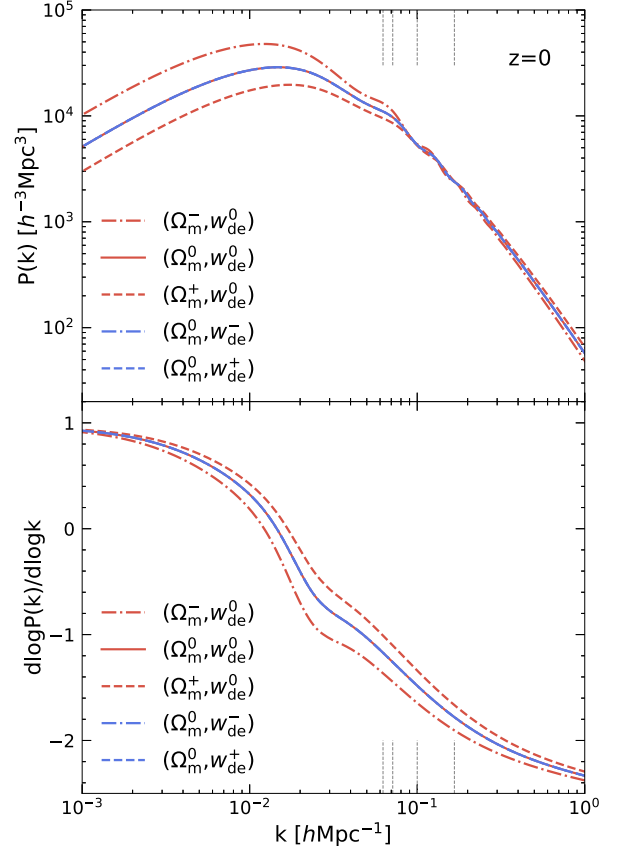


Figure B1. Linear matter power spectra (upper panel) and their slope (lower panel) for five cosmologies considered. From left to right, the vertical ticks located on $k = 1/R_s$ (grey dashed) mark wavenumbers corresponding to the Gaussian smoothing scales $R_s = 16, 14, 10,$ and $6 h^{-1} \text{Mpc}$, respectively. All power spectra have the identical normalization amplitude σ_8 . Note that the power spectrum slope difference becomes larger on smaller wavenumbers than the smoothing lengths we consider. This implies that one can better constrain Ω_m with a larger smoothing scale.

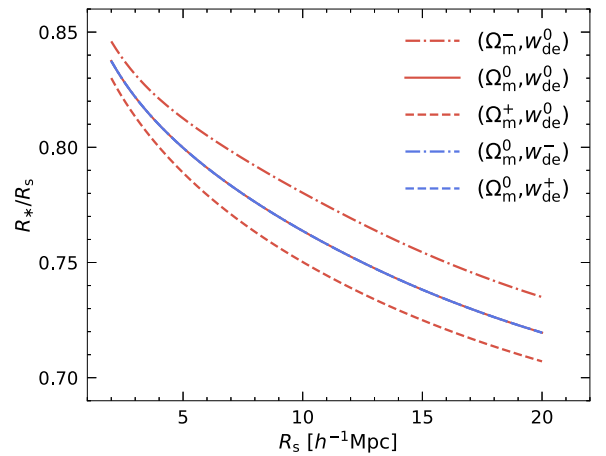


Figure B2. Gaussian prediction for normalized R_* as a function of smoothing scale R_s for five different cosmologies. Ω_m -shifted and w_{de} -shifted cosmologies are shown in red and blue lines, respectively. Note that the predictions for the w_{de} -shifted models (blue) perfectly overlap with the fiducial case (red solid). Note also that the moment ratios of a given power spectrum are redshift independent.

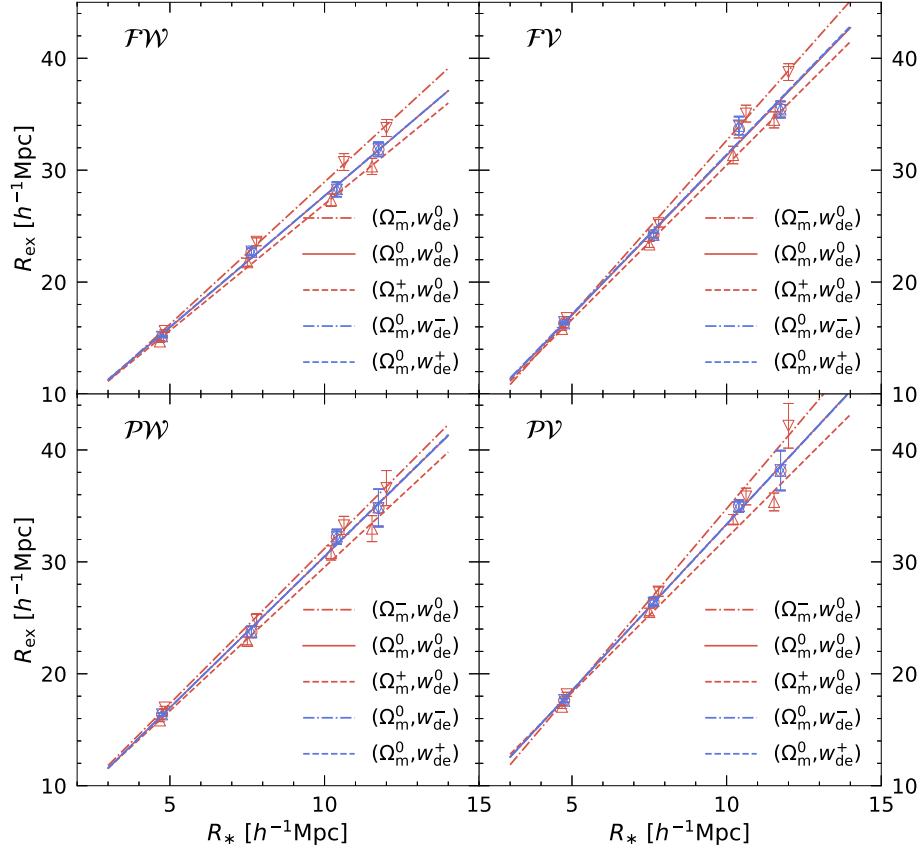


Figure B3. Relation between the measured exclusion radius R_{ex} and the predicted R_* for four different cross-correlation functions. Symbols from left to right correspond to the measurements and Gaussian predictions at smoothing scales $R_s = 6, 10, 14,$ and $16 h^{-1}\text{Mpc}$. Best linear fits for the symbols are shown in lines and the coefficients of the fits are given in Table B1. Again, error bars represent the standard errors of the mean.

the power spectrum slope, n_s at that scale (equation 11), we can interpret its matter density dependence as follows. Because the power spectrum amplitude σ_8 is fixed across different cosmologies, a power spectrum with larger Ω_m has less large- and more small-scale power, as depicted in Fig. B1. Hence, increasing Ω_m results in a shallower power spectrum slope on scales corresponding to the smoothing lengths considered in this analysis. Thus, R_* , tracing the slope, decreases with increasing Ω_m . It is worth noting that the amplitude of the power spectrum grows over time. The rate of growth is influenced by both Ω_m and w_{de} . However, R_* is expected to remain nearly constant with redshifts given that the growth factors in the moment ratio essentially cancel out.

With both measurements and predictions available, Fig. B3 illustrates the relation between the measured R_{ex} for four distinct cross-correlations and the predicted R_* in the Gaussian random field limit.

The symbols denote measurements at smoothing scales of $R_s = 6, 10, 14,$ and $16 h^{-1}\text{Mpc}$, while the lines represent their respective best fits. Standard errors of the mean are shown with the error bars. The relation between R_{ex} and R_* can be effectively characterized by a linear relation,

$$R_{\text{ex}} = a_1 R_* + a_2, \quad (\text{B1})$$

with its coefficients detailed in Table B1. The slope of the linear scaling relation shows its dependence on the matter density parameter but remains unaffected by changes in the dark energy EOS. Notably, in all cross-correlations, the slope becomes steeper with a smaller Ω_m .

This paper has been typeset from a $\text{\TeX}/\text{\LaTeX}$ file prepared by the author.